Evaluation of Conventional Radio Frequency Interference Detection Algorithms in the Presence of 5G Signals in a Controlled Testbed

Ahmed Manavi Alam⁽¹⁾, Md Mehedi Farhad⁽¹⁾, Walaa AlQwider⁽¹⁾,

Vuk Marojevic⁽¹⁾, Mehmet Kurum⁽²⁾, and Ali C. Gurbuz⁽¹⁾

(1) Dept. of Electrical and Computer Engineering, Mississippi State University, Mississippi State, MS

(2) University of Georgia, Athens, GA, USA

{aa2863, mf1413, wq27}@msstate.edu, vuk.marojevic@ece.msstate.edu, kurum@uga.edu, gurbuz@ece.msstate.edu

Abstract-Emerging communication services and satellite system deployments pose heightened interference challenges for crucial passive radiometer sensors used in environmental and atmospheric sensing. Therefore, there is an urgent necessity to develop effective approaches for detecting, mitigating, and characterizing the influence of anthropogenic sources, commonly referred to as radio frequency interference (RFI) on passive Earth-observing microwave radiometers. Experimenting the coexistence of active communication and passive sensing systems would greatly benefit from a thorough and realistic dataset covering a wide range of scenarios. The insufficient availability of extensive datasets in the radio frequency (RF) domain, particularly in the context of active/passive coexistence, poses a significant obstacle to progress. This limitation is particularly notable in the context of comprehending the effectiveness of conventional model-based RFI detection approaches when applied to advanced 5th-generation (5G) wireless communication signals. This study first shows the development of an experimental passive radiometer and 5G testbed system and aims to assess the efficacy of the widely employed spectral kurtosis RFI detection approach within controlled anechoic chamber experiments. Our experimental setup comprises a fully calibrated SDR-based Lband radiometer subjected to diverse 5G wireless signals, varying in power levels, frequency resource block group allocation, and modulation techniques. Significantly, our testbed facilitates the concurrent recording of ground truth temperatures while subjecting the radiometer to 5G signal transmission which helps to understand the overall effect in the radiometer. This distinctive configuration provides insights into the effectiveness of traditional RFI detection models, offering valuable perspectives on the associated challenges in RFI detection.

Index Terms—Microwave radiometer, remote sensing, deep learning, RFI, 5G, active-passive spectrum coexistence

I. INTRODUCTION

The wireless spectrum is a vital and finite resource that significantly influences daily life, playing an essential role in both Earth observation and active wireless communication [1]. It plays a crucial role in mobile broadband, weather forecasting, astronomy, and space exploration [2]. This synergy becomes evident as technologies overlap in frequency bands, serving both active communication and passive observation

This work was supported by the National Science Foundation under Grant No. 2332661 and 2332662.

needs, underscoring their interconnected nature for the benefit of humanity. In Earth observation, passive radiometers play an important role by converting natural thermal radiation into brightness temperature (T_B) , crucial for deriving geophysical parameters like soil moisture, ocean salinity, and atmospheric water vapor [3]. These sensors, requiring no physical contact, ensure precise and non-intrusive measurements of environmental variables. Their heightened sensitivity enables the detection of slight changes in thermal emission. However, challenges arise from radio frequency interference (RFI), primarily caused by anthropogenic signals such as active wireless communications. RFI introduces bias into calibrated radiometric data, affecting the accuracy of geophysical parameter estimates and posing a threat to Earth observation endeavors.

In this study, spectral kurtosis [4], a conventional RFI detection method, has been tested on a controlled anechoic chamber radiometer dataset. This physical testbed consists of a customizable 5G new radio (NR) system that may broadcast wireless communication signals and is presented together with a calibrated L-band radiometer that is akin to those used in satellite-based Earth observation for remote sensing. Researchers can use this experimental dataset to further assess how well algorithms for RFI detection, identification, classification, mitigation, and spectrum coexistence work [5]. This study is primarily dedicated to the identification of RFI in time-frequency spectrograms, aiming to eliminate contaminated frequency segments and utilize the unaffected portions for scientific purposes. Our investigation reveals that while spectral kurtosis effectively identifies RFI within a spectrogram, the substantial power transmission from 5G could amplify the overall impact on radiometers, potentially introducing bias to measurements. Our future studies will aim to evaluate more conventional and data-driven approaches for RFI detection and mitigation to enhance the reliability of radiometer measurements both in chamber and outdoor environments [6]–[8].

The paper is structured as follows: Section II presents the spectral kurtosis algorithm. The whole testbed and the experimental scenarios and data processing are discussed in Sections III and IV respectively. Section V provides the Finally, conclusions are drawn in Section VI.

II. RFI DETECTION WITH SPECTRAL KURTOSI

Spectral kurtosis is a statistical tool to find non-Gabehavior in a fixed number of samples. It has been adapted in RFI detection and mitigation through the I domain transformation. We start with computing the sho Fourier transform (STFT) of the received signal x(t) a

$$S(f,\tau) = \int_{-\infty}^{\infty} x(t) \cdot w(t-\tau) \cdot e^{-j2\pi f t} dt.$$

where $S(f,\tau)$ is the STFT of x(t), $w(t-\tau)$ is the v function centered at time τ , and f represents the free To calculate spectral kurtosis estimator SK(f) [4], [9] according and fourth order moments are computed as

$$M_2(f) = \sum_{\tau} |S(f,\tau)|^2, \quad M_4(f) = \sum_{\tau} |S(f,\tau)|^4, \quad (2)$$

which are utilized further to estimate final spectral kurtosis SK(f) defined in (3).

$$SK(f) = \left(\frac{N+1}{N-1}\right)\left(N\frac{M_4}{M_2^2} - 1\right). \tag{3}$$

where N is the total number of time samples in $S(f, \tau)$.

In the context of the Binary Hypothesis criterion, the detector stage is tasked with deciding between two hypotheses in the transformed domain. Specifically, the hypotheses are stated as follows. H_0 : The sample is considered RFI clean, represented as $SK_{no-RFI}(f)$. This is calculated from the radiometer samples inside the anechoic chamber that is not contaminated by RFI. H_1 : The sample is marked as RFI-contaminated, represented as $SK_{RFI}(f)$. This is derived from contaminated radiometer samples.

The decision is made by comparing the estimated SK(f) in each frequency bin with a predetermined threshold value α . The threshold value α is determined by setting a probability of false alarm (P_{FA}) a priori. P_{FA} is defined as the probability of erroneously choosing hypothesis H_1 when the true hypothesis is H_0 , equivalently $P_{FA} = P(H_1|H_0)$. Your specific α is set to achieve a 0.3% false alarm rate, and it is applied with both upper (α_u) and lower threshold criteria (α_l) . This ensures that the decision process maintains a controlled probability of false alarms during the hypothesis testing for RFI contamination. The decision rule is formulated as follows:

$$\begin{cases} \text{Choose } H_0 & \text{if } \alpha_l < SK(f) < \alpha_u \\ \text{Choose } H_1 & \text{otherwise} \end{cases}$$

More details on establishing the threshold with respect to L-band radiometer will be illustrated in Section IV-B.

III. OVERALL TESTBED

A. Experimental Setup

The experiment setup includes a 5G transmitter and an L-band microwave radiometer as passive receiver [5], [10]. The experiment is conducted inside a radio-neutral zone (anechoic

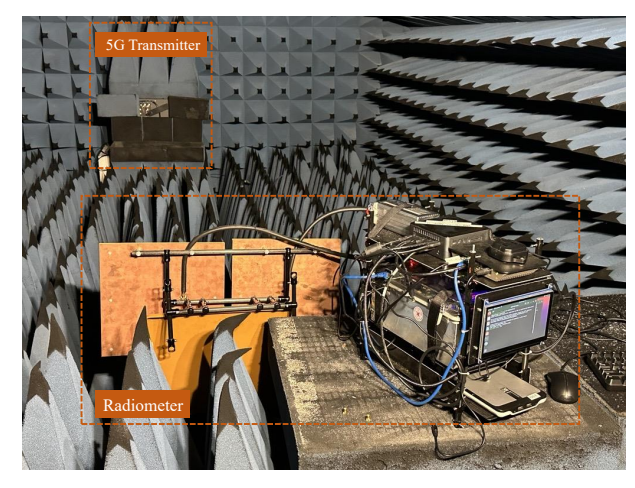


Fig. 1: Experimental setup illustrating the 5G signal transmitter and L-band radiometer configuration within the anechoic chamber.

chamber) at Mississippi State University. The arrangement of the dual-polarized L-band radiometer receiver antenna and the 5G transmitter antenna was designed to ensure an unobstructed line of sight between them, as illustrated in Fig. 1. The 5G transmitter was remotely controlled during the experiment to reduce any unwanted bias. Within the anechoic chamber, the radiometer antenna was placed at the front position, while the 5G transmitter antenna was situated at the back. The ambient temperature in the anechoic chamber was rigorously regulated and maintained at a consistent level throughout the experiment.

B. 5G Transmission System

The 5G NR waveforms were formulated utilizing MAT-LAB's 5G Toolbox, adhering to the most recent specifications outlined by the 3rd Generation Partnership Project (3GPP). This toolbox facilitates the generation of a comprehensive 5G waveform, encompassing the entire transmission link, which includes channel encoding, modulation, and Multiple Input Multiple Output (MIMO) precoding. We modified the waveform generation to control transmission parameters such as resource block allocation in the frequency domain, slot and symbol positioning in the time domain, modulation schemes, transmission power levels, and channel coding rates. These adjustments were made to align with our experimental objectives. After generation, the complex In-phase and Quadrature (IQ) samples undergo conversion into a binary format using MATLAB's dedicated function, a crucial step for the subsequent over-the-air transmission process [11].

Our design utilizes GNU Radio with a Software Defined Radio (SDR) device—specifically, the Universal Software Radio Peripheral (USRP) B210 model—for over-the-air transmission. The USRP B210 acts as the bridge between the digital and analog RF worlds. It supports a broad RF spectrum ranging from 70 MHz to 6 GHz and boasts an instantaneous bandwidth of up to 56 MHz. Further details about the 5G transmitter testbed can be found in our previous publications [5], [12].

1) 5G Frame and Carrier Structure: In 5G networks, time frames are typically segmented into 10 ms intervals, known as subframes, in accordance with the 5G specifications [13]. These subframes are further divided into smaller units called slots, which consist of OFDM (Orthogonal Frequency-Division Multiplexing) symbols, representing the smallest scheduling units within this time frame architecture. In 5G, time frames are 10 ms subframes. Subcarrier spacing (SCS) regulates subcarrier frequency, impacting data transmission efficiency. 5G NR offers a range of SCS options, including 15, 30, 60, 120, and 240 kHz. The structure of an NR subframe, encompassing the number of slots and the duration of each OFDM symbol, is governed by the chosen SCS. Employing longer SCS results in shorter slot duration, thus allowing more slots per subframe. Despite SCS variations, subframes maintain a fixed duration of 1 ms, with each slot usually comprising 14 OFDM symbols. In the frequency domain, the organization of 5G networks is outlined by the frequency resource grid. The smallest unit within this grid is the resource element (RE), defined by the intersection of an OFDM symbol in the time domain and a subcarrier in the frequency domain. A resource block (RB), consisting of 12 consecutive REs, is the smallest frequency resource unit that can be allocated to a user for a specified transmission time interval (TTI). This allocation is dynamic, allowing for adaptation to the varying data needs of different users. Notably, the bandwidth of an RB depends on the chosen SCS; wider SCS values lead to larger RBs. Furthermore, RBs are aggregated into resource block groups (RBGs). The size of an RBG, determined by a higher-layer protocol, consists of 'P' RBs, with the minimum value of 'P' being 2.

2) Preliminary 5G power experiment: During waveform generation, we adjusted signal power by specifying the power gain. To assess the relationship between set power gain and received signal power, we conducted experiments focusing on the 5G transmitter, excluding the radiometer. The signal was transmitted via a coaxial cable and captured by a spectrum analyzer connected to the transmitter's USRP B210, linked to a PC running GNU Radio for signal transmission. We generated a variety of waveforms, differing in the number of allocated RBGs and power gain settings. On the receiver's side, we measured the average power of the received signal for each configuration. The outcomes of these measurements are detailed in Table 1. Analysis of the data reveals a clear trend: increasing the power gain leads to an increase in the average received power levels, uniformly across all tested RBG allocations. Furthermore, increasing the number of allocated RBGs exhibited a marginal impact on the measured power of the received signal.

C. L-Band Radiometer

We construct a passive receiver employing an L-band microwave radiometer [14] to assess the impact of 5G transmissions on passive remote sensing. This system functions within the 1400-1427 MHz range of the RF spectrum, having a 27 MHz bandwidth.

TABLE I: Transmitted Power Estimation in 5G

RBGs	Power gain (dB)	Avg Power (dBm)	RBGs	Power gain (dB)	Avg Power (dBm)
2	-20	-51	8	-20	-47
	-10	-42		-10	-38
	0	-32		0	-29
	10	-22		10	-19
	20	-16.11		20	-15
4	-20	-48.5	16	-20	-47
	-10	-41.9		-10	-38
	0	-32.2		0	-28
	10	-21.5		10	-17.6
	20	-15.7		20	-13.8

1) Radiometer Design Schematic: The radiometer's hardware architecture is divided into three main components: RF front-end, digital back-end, and receiving antenna. In the RF front-end, a single-pole four-throw (SP4T) RF relay is employed, optimized for the 1-3 GHz frequency band. This relay enables 250 ms time delays for each through connection via external triggering. Both H-pol and V-pol antennas are connected to the RF relay's 1st and 2nd port, while the 3rd and 4th ports are connected to a 50-ohm matched load (HS or ambient source) and a reverse low-noise amplifier (LNA) terminated with a 50-ohm matched load (active cold source, ACS) respectively. The connectivity involves these ports being linked to the dual-polarized antenna and reference loads, succeeded by a 20 dB RF isolator that ensures unidirectional signal flow within the 1-2 GHz frequency range. Following the isolator, there is a custom-designed bandpass (BP) RF filter, operational from 1400 MHz to 1427 MHz with a center frequency of 1413.5 MHz, and subsequently another LNA operating from 1.2 GHz to 1.6 GHz. The entirety of the RF frontend, positioned on a temperature-controlled aluminum plate, maintains consistent performance by minimizing stochastic variations in noise levels. Our custom-built digital back-end leverages a highly versatile National Instruments USRP B210 as a software-defined radio (SDR). This allows for real-time digitization of the incoming RF signal at 30 MHz, directly from the front-end's LNA. An Intel Next Unit of Computing (NUC) mini PC serves as the brain, seamlessly managing data acquisition and storage. Two Raspberry Pis handle specific tasks: one orchestrates the SP4T RF relay for efficient port switching (250 ms integration time), while the other meticulously monitors temperatures of all critical components, including the dual-polarized antenna and coaxial cables. To mitigate the impact of temperature fluctuations, a dedicated controller unit utilizes a Peltier cell to maintain stable frontend conditions, ensuring pristine radiometric measurement accuracy.

2) Radiometer Calibration: To establish the accuracy and stability of our radiometer's T_B measurements, we employed a multifaceted calibration procedure. This involved referencing three well-characterized external sources: liquid nitrogen (LN), dry ice (DI), and a hot source (HS). Additionally, we continuously monitored the TB of a blackbody (anechoic chamber walls) and the sky for an hour to assess calibration stability. The internal temperature was maintained at 305.15 K throughout the experiment. The system noise temperature (T_{sys}) was determined to be 537.1 K utilizing the Y-technique

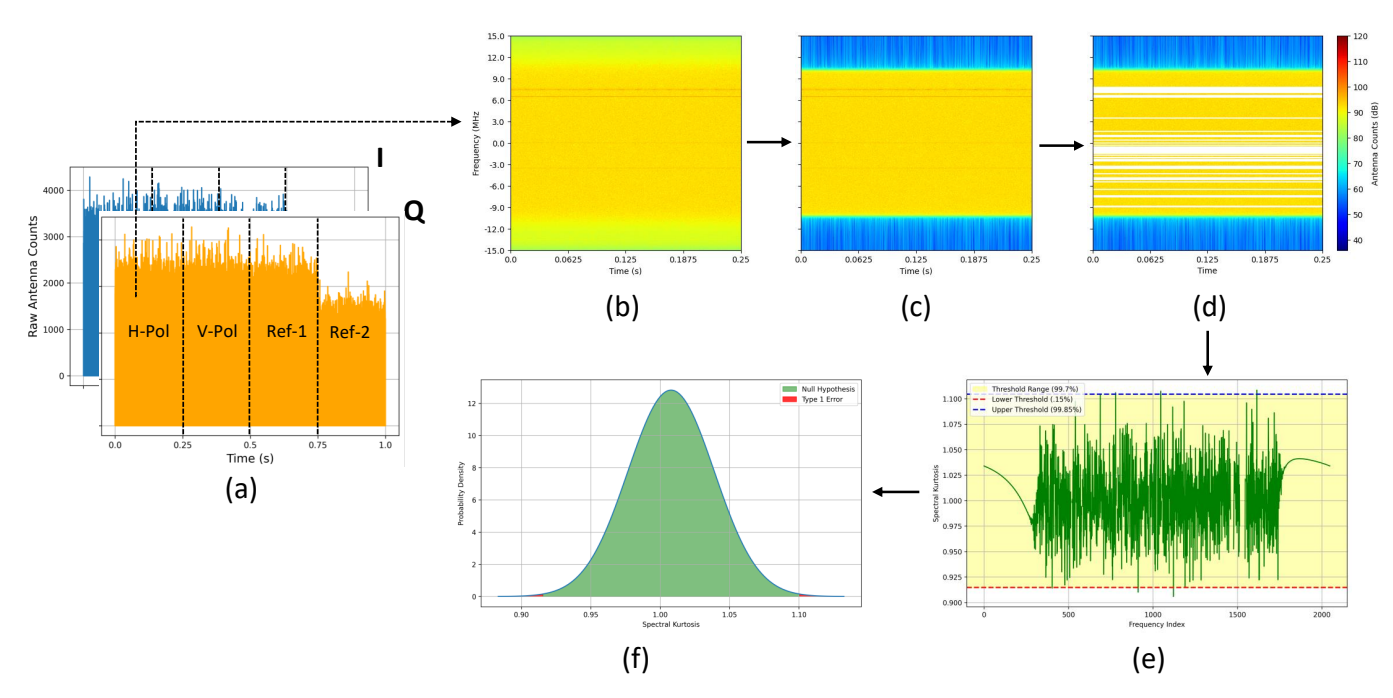


Fig. 2: Data pre-processing steps for radiometer. a) Raw IQ samples received from the radiometer. A single sample has 1s of integration time with H-pol, V-pol, ref1, and ref2. Each state consists of 0.25 s integration time. b) PSD and Spectrograms of received IQ samples before filtering, c) after filtering, d) internal RFI removed e) spectral kurtosis after pre-processing and f) PDF of spectral kurtosis to estimate threshold.

with LN and DI sources as described in [3]. This translates to a total noise figure (NF) of 4.4 dB. Based on T_{sys} , bandwidth (27 MHz), and integration time (250 ms), the theoretical noise equivalent delta temperature (NE Δ T) is calculated as 0.21 K. Additional details on radiometer calibration and system performance can be found in [10].

IV. METHODOLOGY

A. Experiment Scenario

The experimental setup encompasses various scenarios, each involving an examination of the impacts of 5G waveforms on radiometric systems. 5G waveforms are purposefully transmitted within the radiometer's working bandwidth (1400-1427 MHz) to develop an in-band experiment. The experimental configuration includes multiple scenarios, each entailing an in-depth exploration of the impact of 5G waveforms on radiometric systems. Various gain settings are used for 5G transmissions, ranging from -20 dB to 20 dB in 10-step increments. Three different modulation schemes are used in the trials along with changes in frequency and gain: 64QAM, 16QAM, and Quadrature Phase Shift Keying (QPSK). The study's scope is expanded by the incorporation of several modulation schemes, which enables a wider investigation of the ways in which various modulation approaches contribute to the impacts on radiometric measurements that have been reported. Additionally, various combinations of RBGs allocation are included in transmitted signals to understand the efficacy of RFI detection algorithms.

B. Data Pre-Processing and Threshold Estimation

Effective data pre-processing is essential for establishing a threshold in RFI detection as it significantly improves result quality and reliability by addressing issues such as noise, outliers, and inconsistencies. This ensures accurate capture of underlying patterns and trends in the data. In this section, we present a workflow to eliminate internal bias and establish threshold α in binary hypothesis criterion discussed in Section II. Fig. 2(a) illustrates IQ samples of a complete cycle (1000 ms), comprising four segments. The first two segments represent H-pol and V-pol, reflecting antenna observations of the scene. The third and fourth segments display responses from internal reference loads (Ref-1 and Ref-2 for HS and ACS, respectively). Fig. 2(b) depicts spectrograms of uncalibrated raw IQ samples with no 5G transmission. These domain transformations reveal undesired biases and spikes in the radiometer data when no transmission occurs within the anechoic chamber. Potential culprits for these biases include internal electronic and RF instruments. To address this issue, we design a Butterworth low-pass filter with a high order of 28 and a cutoff frequency of 10 MHz. This filter attenuates higher frequency components, allowing only signals below 10 MHz to pass through with minimal distortion, as illustrated in Fig. 2(c). Additionally, an internal RFI detection algorithm is developed within the filtered region to eliminate any unwanted biases from the data. An outlier mask is generated by analyzing 200 different no-RFI (with no transmission) samples to identify contaminated frequency bins. This outlier mask is uniformly applied across all samples to ensure consistency throughout

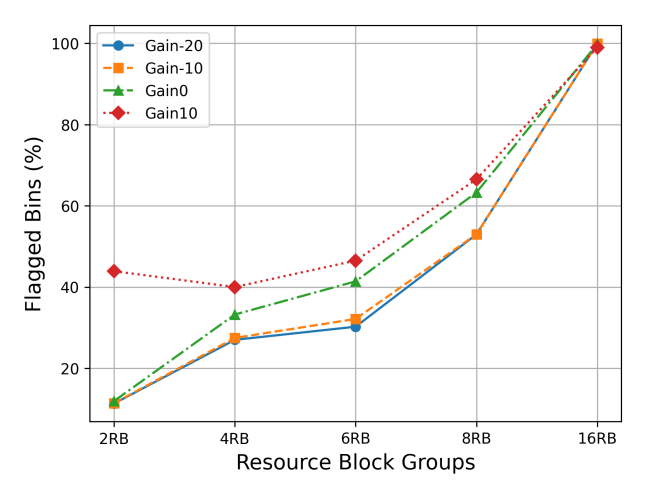


Fig. 3: Flagged time-frequency bins with spectral kurtosis for various signal gains and RBGs for H-pol.

the dataset. The resulting samples, after internal RFI removal (IRR), are depicted in Fig. 2(d). After this process, spectral kurtosis is estimated from 3. This is illustrated in Fig. 2(e). Probability density function (PDF) of estimated spectral kurtosis is illustrated 2f. This shows the acceptable region for H_0 and establishment of decision threshold with 0.3% false alarm rate.

C. Quantifying Impact of 5G transmission

This section introduces the evaluation metrics for assessing the impact of 5G-induced RFI on the L-band radiometer. The study observes in-band transmissions in a controlled anechoic chamber with highly absorbing materials. These materials, with high emissivity, ensure the radiometer-measured brightness temperature approximates the antenna's physical temperature. The anechoic chamber's high absorbance and non-reflective properties enable a direct attribution of observed effects to the transmission. For both in-band and out-of-band emissions, the impact on the radiometer is characterized by the temperature difference (ΔT) given by the expression $\Delta T = T_{\rm RFI} - T_{\rm No-RFI}$. Here, $T_{\rm No-RFI}$ is directly calculated from the antenna temperature, serving as the ground truth, and $T_{\rm RFI}$ represents the RFI-contaminated brightness temperature estimated through radiometer internal and external calibration.

V. RESULTS

A. Overall Performance

In this section, overall performance in detecting and mitigating RFI in an L-band radiometer will be illustrated. RFI sources are 5G NR signals with different RBGs and power levels. In Fig. 3, flagged time-frequency bins for a particular sample are depicted with different RBGs and power levels. With higher number of resources occupied within the spectrum results in a higher number of flagged time-frequency bins. For a specific RBG allocation, higher power gain level also results in a higher number of corrupted measurements within a sample. As gain increases, the system may operate closer to the upper limit of its dynamic range, contributing to contaminated

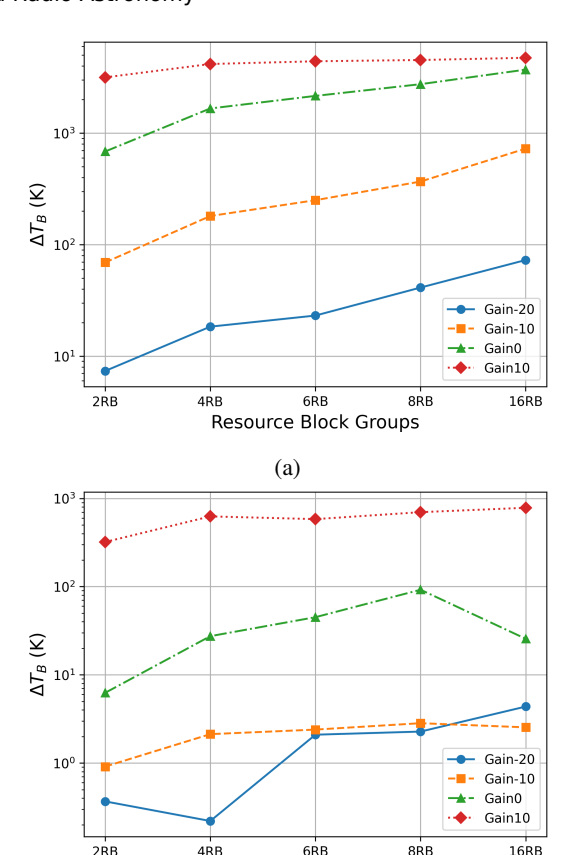


Fig. 4: Effects of RFI in radiometer with in-band transmissions with different RBGs and power gain a) before RFI removal b) after RFI removal

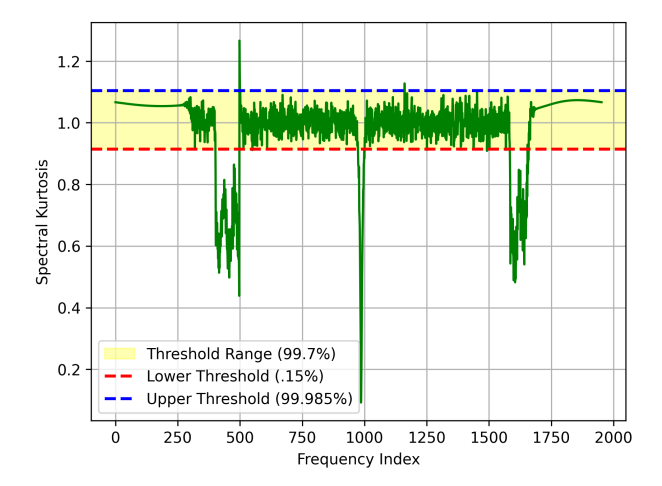
(b)

Resource Block Groups

measurements. Moreover, high power transmitters can cause power leakage to adjacent frequency bins which results in a higher number of flagged bins by the detection algorithm. This phenomenon could be attributed to imperfect filtering from the transmitter side. Consequently, it is imperative to consider important filtering techniques during in-band transmissions, particularly when a higher number of RBGs are allocated for the 5G transmission. Figure. 4(a) and 4(b) illustrate the overall effect in radiometer compared with ground truth information before and after RFI removal respectively. Comparing ΔT_B with both cases shows overall affect has been significantly reduced in the radiometer. The presence of raw IQ samples has enabled the application of advanced domain transformation techniques, facilitating the recovery of time-frequency bins within specific samples. Nonetheless, the impact on ΔT_B as depicted in Fig. 4(b) indicates that the radiometer is affected to a lesser extent by missed RFI detection cases at lower power levels compared to higher power levels. The high power gain levels contribute to higher T_B , and improper detection of RFI in such high-power gain scenarios could significantly impact the overall measurements. This observation suggests that conventional RFI detection algorithms, such as spectral kurtosis, may face challenges in effectively addressing the characteristics of 5G signals, especially during high-power gain transmissions. Future studies will utilize Receiver Operating Characteristic (ROC) curves to examine how the probability of detection varies in relation to the false alarm rate.

B. Challenges with Conventional Method

This section will illustrate an example case of RFI contaminated radiometer sample and how spectral kurtosis is utilized to detect and mitigate the anthropogenic signal effect. Fig. 5(a) displays the spectral kurtosis of the measurement, captured under conditions of 2RBG and a power level of -10 gain. Fig. 5(b) and (c) illustrate the fully calibrated T_B spectrogram before and after RFI removal respectively. While spectral kurtosis effectively eliminates the majority of contaminated portions, the detection algorithm tends to overlook frequency bins adjacent to the RBG bandwidth. This oversight results in an overall bias in the measurements, indicated by $\Delta T_B = 0.92 K$. This highlights the need for more advanced RFI detection algorithms that can leverage both time-frequency properties are required to detect RFI.



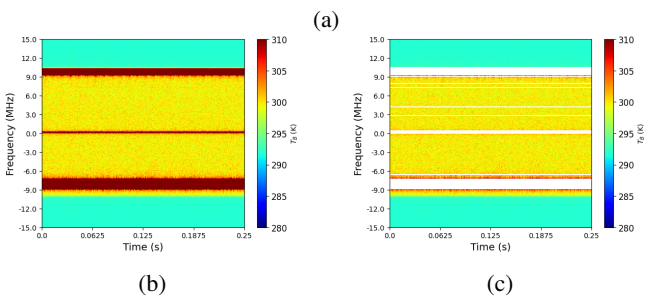


Fig. 5: a) Spectral kurtosis of RFI contaminated sample. Spectrogram a) before and c) after RFI removal with 2RBG and gain -10. Measured T_B after RFI removal is 297.3633 K and ground truth T_B is 296.45 K

VI. SUMMMARY AND CONCLUSION

This study demonstrates the evaluation of the widely used spectral kurtosis RFI detection approach in the presence of 5G signal transmission within a controlled anechoic chamber.

Our results demonstrate the overall effectiveness of spectral kurtosis in mitigating RFI in an L-band radiometer exposed to diverse 5G signal. However, challenges arise, particularly at higher power levels, where conventional RFI detection algorithms may exhibit limitations, leading to potential biases in measurements. The impact of missed RFI detection cases is more pronounced in high-power gain scenarios, highlighting the need for advanced RFI detection algorithms capable of addressing the unique characteristics of 5G signals. Future studies will emphasize integrating more RFI detection algorithms for both internal chambers and external environments.

REFERENCES

- [1] I. F. Akyildiz, W.-Y. Lee, M. C. Vuran, and S. Mohanty, "A survey on spectrum management in cognitive radio networks," *IEEE Communications magazine*, vol. 46, no. 4, pp. 40–48, 2008.
- [2] L. Palen, M. Salzman, and E. Youngs, "Discovery and integration of mobile communications in everyday life," *Personal and ubiquitous* computing, vol. 5, pp. 109–122, 2001.
- [3] F. T. Ulaby, R. K. Moore, and A. K. Fung, "Microwave remote sensing: Active and passive. volume 1-microwave remote sensing fundamentals and radiometry," 1981.
- [4] J. Taylor, N. Denman, K. Bandura, P. Berger, K. Masui, A. Renard, I. Tretyakov, and K. Vanderlinde, "Spectral kurtosis-based rfi mitigation for chime," *Journal of Astronomical Instrumentation*, vol. 8, no. 01, p. 1940004, 2019.
- [5] W. Al-Qwider, A. M. Alam, M. Mehedi Farhad, M. Kurum, A. C. Gurbuz, and V. Marojevic, "Software radio testbed for 5g and 1-band radiometer coexistence research," in *IGARSS 2023 2023 IEEE International Geoscience and Remote Sensing Symposium*, 2023, pp. 596–599.
- [6] A. M. Alam, M. Kurum, and A. C. Gurbuz, "Radio frequency interference detection for smap radiometer using convolutional neural networks," *IEEE Journal of Selected Topics in Applied Earth Observations and Remote Sensing*, vol. 15, pp. 10099–10112, 2022.
- [7] A. M. Alam, M. Kurum, M. Ogut, and A. C. Gurbuz, "Microwave radiometer calibration using deep learning with reduced reference information and 2-d spectral features," *IEEE Journal of Selected Topics* in Applied Earth Observations and Remote Sensing, vol. 17, pp. 748– 765, 2024.
- [8] A. M. Alam, M. Kurum, and A. C. Gurbuz, "High-resolution radio frequency interference detection in microwave radiometry using deep learning," in *IGARSS* 2023 - 2023 IEEE International Geoscience and Remote Sensing Symposium, 2023, pp. 6779–6782.
- [9] G. M. Nita, D. E. Gary, and G. Hellbourg, "Spectral kurtosis statistics of quantized signals," in 2016 Radio Frequency Interference (RFI). IEEE, 2016, pp. 75–80.
- [10] M. M. Farhad, A. M. Alam, S. Biswas, M. A. S. Rafi, A. C. Gurbuz, and M. Kurum, "Sdr-based dual polarized l-band microwave radiometer operating from small uas platforms," *IEEE Journal of Selected Topics* in Applied Earth Observations and Remote Sensing, 2024.
- [11] T. M. Inc., "Matlab version: 9.13.0 (r2022b)," Natick, Massachusetts, United States, 2022. [Online]. Available: https://www.mathworks.com
- [12] W. Alqwider, A. Dahal, and V. Marojevic, "Software radio with matlab toolbox for 5G NR waveform generation," in 2022 18th International Conference on Distributed Computing in Sensor Systems (DCOSS), 2022, pp. 430–433.
- [13] The 3rd Generation Partnership Project (3GPP) "NR; Physical channels and modulation," Technical specification (TS) 38.211, 2022, Version 17.1.0.
- [14] M. M. Farhad, S. Biswas, A. M. Alam, A. C. Gurbuz, and M. Kurum, "SDR based agile radiometer with onboard rfi processing on a small uas," in *IGARSS* 2023 - 2023 IEEE International Geoscience and Remote Sensing Symposium, 2023, pp. 4368–4371.